The Marshall Plan Scholarship Paper

Fluid-structure interaction simulations of patient-specific aortic dissection with advanced material models

Author:

- Malte Rolf-Pissarczyk
  Institute of Biomechanics, Graz University of Technology, Austria

Contributions:

- Kathrin Bäumler
  3D and Quantitative Imaging Laboratory, Department of Radiology, Stanford University, CA, USA
- Richard Schussnig
  High-Performance Scientific Computing, University of Augsburg, Germany
- Thomas-Peter Fries
  Institute of Structural Analysis, Graz University of Technology, Austria
- Alison L. Marsden
  Department of Pediatrics and Bioengineering, Stanford University, CA, USA
- Dominik Fleischmann
  3D and Quantitative Imaging Laboratory, Department of Radiology, Stanford University, CA, USA
- Gerhard A. Holzapfel
  Institute of Biomechanics, Graz University of Technology, Austria
  Department of Structural Engineering, Norwegian University of Science and Technology, Norway

Sep 1st, 2022 – Nov 31st, 2022

Abstract

Aortic dissection is a life-threatening condition, characterized by the abrupt formation of a new parallel flow channel, the false lumen. Degeneration and aneurysm formation of the false lumen in the chronic phase of the disease are the main cause for late complications and death. The interplay between anatomic remodeling, hemodynamics and wall stress over the course of the disease are not yet well understood. We present a numerical framework to investigate the evolution of a patient's aortic dissection, captured by surveillance imaging with computed tomography angiography from the subacute phase to five years after disease onset. However, the subject of this report is only the examination of a single computed tomographic angiography image of the patient's aortic dissection. A two-way fluid–structure interaction model is implemented in the open-source software SimVascular allowing for the implementation of varying wall thicknesses, prestresses, external tissue support and anisotropic material properties of the dissected aorta. The aortic geometry, in vitro four-dimensional flow magnetic resonance imaging and the patient's blood pressure are used to then apply in vivo boundary conditions. This allows us to study the interplay between deformation of the aorta and the hemodynamics in the diseased aorta. Furthermore, to describe the microstructure of the pathological aortic wall, an anisotropic material is implemented in open-source software SimVascular, followed by the required verification activities. Later, the dependency of the result on anisotropic material models can be examined in comparison to a simple isotropic model. In the future, it is also planned to examine further follow-up computed tomography angiography images of this particular patient.

1 Introduction

Aortic dissection is a relatively uncommon but a highly lethal condition of the cardiovascular system, with incidences ranging from 3 to 8 cases per 100 000 persons [15, 10]. Dissections are often accompanied by severe chest or back pain and acute hemodynamic compromise [35]. When untreated, medical studies have shown that the mortality rate of type A aortic dissections according to the Stanford classification [15] increases by 12 % per hour within the first 24 h upon reaching hospital, as a result, mortality rates of up to $50 - 74$ % within the first 2 weeks have been observed [10, 15]. Estimates suggest that even 40 % are fatal prior to arrival [16]. In contrast, an uncomplicated, acute, type B aortic dissection is usually less lethal, with survival rates of up to 89 % in medically treated patients at 1 month and 80 % after 5 years [16]. Usually, aortic dissection is initiated by a small tear at the inner layer of the aorta, which then gradually propagates within the aortic layers leading to a so-called false lumen. The presence of a false lumen changes the local hemodynamics in the aorta, and consequently causes tissue remodeling (degradation) and thrombus formation. To fully study the initiation and progression of aortic dissection, the mechanical behavior of the pathological aortic wall under the impact of blood flow must be investigated. This can be evaluated by means of fluid–structure interaction (FSI) simulations.

FSI, which combines computational fluid dynamics (CFD) and computational structural dynamics play a major role in appropriate modeling of blood flow. Blood vessels act as compliant tubes that change size dynamically when there are changes to blood pressure and velocity of flow. FSI modeling is the only modeling approach allowing to study an interaction between blood flow, arterial wall material properties and arterial wall geometry. In other words, the three entities involved in the process of pathological vessel wall development, such as atherosclerosis, thrombus formation, development of aneurysms or aortic dissection.

Only a few FSI simulations of patient-specific aortic dissection have been published in the literature, see, e.g., [2, 60, 59, 1], because simulations are still challenging for two reasons. First, the complex geometry of an aortic dissection, in which the true and the false lumen are separated by a more or less stable dissection flap, leads to complex flow patterns and an inhomogeneous stress distribution in the aortic wall with high stress gradients. This means that the computational effort is enormous. Second, medical data from aortic dissection patients are rare, especially high resolution medical data. Recently, Bäumler et al. [2] published an outstanding work on a FSI simulation of patient-specific aortic dissection, in which a comprehensive numerical framework for CFD simulations of aortic dissection was developed that captures the complex interplay between physiological deformation and hemodynamic in a patient-specific model. The patient-specific aortic geometry was derived from computed tomography angiography images, which were provided by Prof. Dominik Fleischmann (3D and Quantitative Imaging Laboratory, Department of Radiology, Stanford University, CA, U). In addition, due to the availability of three-dimensional phase-contrast magnetic resonance imaging, blood pressure could be used to define physiologically realistic, patient-specific boundary conditions. Notwithstanding the importance of this study, the model lacks incorporation of the microstructure of the aortic wall. In other words, Bäumler et al. [2] applied an isotropic neo-Hookean model to describe the material behavior of the aortic wall. In fact, the aortic wall shows anisotropic material behavior, i.e. the circumferential direction is usually stiffer than the axial direction, mainly caused by circumstantially oriented collagen fibers.

In this project, an advanced material model reflecting the microstructural composition of the aortic wall will be implemented in the open-source software SimVascular [54] to improve the computational results of FSI simulations of patient-specific aortic dissection. In particular, an advanced material model will be compared with the results of the already implemented neo-Hookean material model, which was applied by Bäumler et al. [2] and assumes an isotropic behavior of the aortic wall. This assumption simplifies the material behavior considerably. Subsequently, by using novel medical data, more precisely computed tomography angiography images of an aortic dissection patient with multiple images per cardiac cycle, a novel FSI simulation of the patient-specific aortic dissection will be developed, which will include the creation of meshes for the solid and the fluid domain, the determination of in vivo boundary conditions, the identification of the model parameters, and the tuning of numerical parameters. The results of this new model will then be validated against available medical data. Note that this report will not fully cover this subject, as stated in the project proposal. Here, only the implementation and verification of the anisotropic material model as well as the numerical framework of the patient-specific FSI model of a patient's aortic dissection including some preliminary results will be presented. Future work will then include solving specific numerical problems, post-processing the results and examining other follow-up computed tomography angiography images of this particular patient.

The report is organized as follows: Section 2 provides background information on aortic dissection and the microstructure of the aorta to improve understanding of the following sections. Section 3 explains the constitutive framework of the introduced anisotropic material model, specifically the discrete fiber dispersion (DFD) method, and demonstrates its implementation in the open-source software SimVascular [54], along with the required verification activities. In Section 4, the model is then applied to patient-specific FSI simulations of aortic dissection in the open-

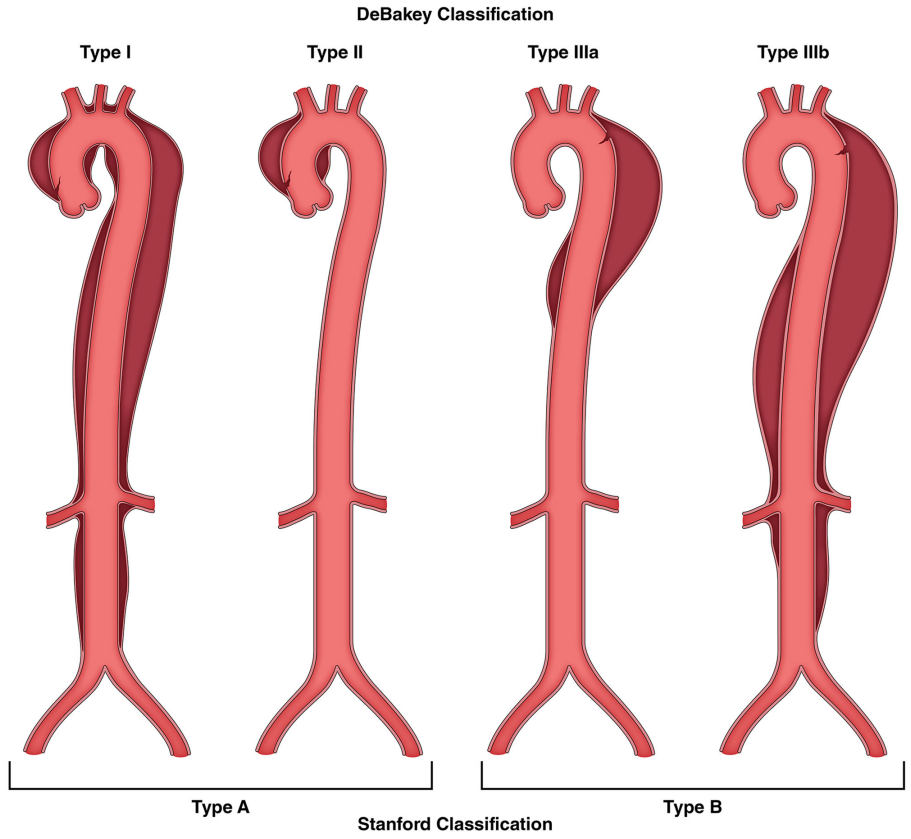

Figure 1: Schematic representative of the DeBakey and the Stanford classification systems, which are the most common systems used. The DeBakey classification system offers great anatomic detail, whereas the Stanford classification system is simpler. It essentially differentiates dissections that involve the ascending aorta from dissections that do not involve the ascending aorta [23].

source software SimVascular [54], utilizing medical data, generated models, and preliminary results and challenges. Lastly, the obtained results are discussed in Section 5.

2 Background

In the following, background information is provided to better understand the content of this report, i.e. the disease aortic dissection and the microstucture of the aortic wall.

2.1 Aortic dissection

Aortic dissection is a complex condition that can be classified into different types. The two major classification methods are the DeBakey classification and the more widely used Stanford classification [23]. Both methods are illustrated in Fig. 1.

The DeBakey classification describes three different types of aortic dissection. Type I aortic dissections originate in the ascending aorta and typically extend through the aortic arch and further. Type II aortic dissections begin and end in the ascending aorta, while Type III aortic dissections begin and end in the descending aorta. Type III can also be further divided into two sub-types: Type IIIa, which is confined to the thoracic descending aorta and does not reach the diaphragm, and Type IIIb, which extends beyond the diaphragm. In contrast, the Stanford classification is simpler and includes just two types: Type A aortic dissections, which include the ascending aorta, the aortic arch, or both, and Type B aortic dissections, which only include the descending aorta. Dissections that originate in the descending aorta and extend into the aortic arch and beyond are also possible.

Aortic dissection can be classified into three phases: Acute, subacute (occurring within the first 90 days of symptom onset), and chronic. While acute aortic dissections receive a lot of attention, chronic aortic dissections are not as well-known [14]. However, more patients are surviving the acute phase and living with a chronic aortic dissection for many years, which requires specialized care and surveillance. Late complications, such as false lumen degeneration and aneurysm formation, often require surgical or endovascular interventions. The need for ongoing

monitoring and specialized medical and surgical care for these patients is becoming a growing healthcare concern.

Open surgical repair is still the most widely used method for treating chronic aneurysmal aortic dissections [14]. This is due to the limitations of current endovascular techniques, such as limitations in the location of the treatment, the non-compliance of the dissection flap, and the uncertain long-term effectiveness of thoracic endovascular aortic repair (TEVAR), as well as the positive effects that recent advancements in surgical techniques, such as improved management of circulation, cerebrospinal fluid drainage, brain and nerve monitoring, and pre- and post-operative protocols have had on surgical outcomes.

2.2 Aortic microstructure in health and disease

The aorta is composed of the three layers intima, media, and adventitia with different structures and functions. The intima is mechanically negligible in young and healthy aortas and consists of a single layer of endothelial cells but becomes mechanically relevant due to non-atherosclerotic thickening with age, where collagen fibers are deposited [21]. The media consists of several concentric lamellar units, where each unit contains smooth muscle cells with their radially tilted longer axes oriented at an angle closer to the circumferential direction and is surrounded by collagen fibrils (Type III) and elastic fibers forming elastic lamellas [33]. The adventitia, the outermost layer, consists mostly collagen fibers (Type I, arranged as two helically fiber families) admixed with a few elastin fibers, nerves, fibroblasts and the vasa vasorum. The media, with two symmetric families of collagen fibers oriented towards the circumferential direction [41], is the main load bearing layer at physiological loads, and the adventitia, with two symmetric families of collagen fibers oriented towards the longitudinal direction [41], acts as a stiff jacket-like tube at higher levels of pressure, which prevents the artery from overstretch and rupture [17]. In the pathological aorta, this complex matrix has found to be altered, which can be modeled with advanced material models that incorporate its anisotropic material behavior.

A key structural change in thoracic aortic dissections is associated with medial degeneration, as first reported by [11]. It involves smooth muscle cell loss, elastic fiber fragmentation, and an accumulation of proteoglycans [9, 5, 58]. A weakened aortic wall due to medial degeneration is also typical for aneurysms of the ascending aorta [8]. Versican and aggrecan were identified as the major components of such accumulations in thoracic aortic aneurysm and dissection patients [7]. Additionally, the elastic fiber structure of a dissected aorta, where the elastic structure connecting the lamellar units are highly degenerated compared to a control aorta [31]. Interestingly, for aortic dissections collagen content was reported to be increased [57, 56, 6] or decreased with an increased disruption [9, 8].

3 Implementation of DFD method in open-source software SimVascular

Currently, there are two main approaches for modeling dispersed fiber distributions in a constitutive equation, namely the "generalized structure tensor" and the "angular integration" approaches [18]. In the angular integration approach [19], the strain energy of a single collagen fiber is assumed to be a function of the fiber stretch. The fiber dispersion in the tissue is incorporated into the strain-energy function by an integration of the single fiber strain energy over all the fiber directions weighted with a continuous probability density function (PDF). As the terminology angular integration is rather imprecise and does not explicitly mention fiber dispersion. Therefore, the terminology "continuous fiber dispersion" is often used instead. If the fiber dispersion is incorporated as a summation of a finite number of discrete fiber contributions, then we refer to this as the "discrete fiber dispersion", or DFD, method. Disadvantages and advantages of the related approaches are described in Li et al. [27]. In the following the DFD method will be detailed and applied for the purposes of this report.

In the following, the constitutive framework is briefly described and then implemented in the open-source software SimVascular [54]. After the implementation, the required verification activities are described in order to apply this model to more comprehensive computational studies later, in particular to FSI simulations of a patient-specific aortic dissection. The described constitutive framework is based on previous works, as described in Rolf-Pissarczyk et al. [38] while the code verification is based on the work of Li et al. [27].

3.1 Constitutive framework of the DFD method

We first introduce the deformation gradient $\mathbf{F}$ relative to a predefined reference configuration. If we consider an incompressible material, we require that the determinant of $\mathbf{F}$, known as the Jacobian J, is equal to unity or $\det\mathbf{F} \equiv 1$. For this model we can now decouple $\mathbf{F}$ into a volumetric (dilatational) part $J^{1/3}\mathbf{I}$ and an isochoric (distortional) part $\overline{\mathbf{F}} = J^{-1/3}\mathbf{F}$, where $\mathbf{I}$ is the second-order unit tensor. The right Cauchy–Green tensor $\mathbf{C} = \mathbf{F}^{\mathsf{T}}\mathbf{F}$ is the basic kinematic variable formulated in the reference configuration, together with its modified counterpart $\overline{\mathbf{C}} = \overline{\mathbf{F}}^{\mathsf{T}}\overline{\mathbf{F}}$ and the corresponding first invariants $I_1 = \operatorname{tr}\mathbf{C}$ and $\bar{I}_1 = \operatorname{tr}\overline{\mathbf{C}}$.

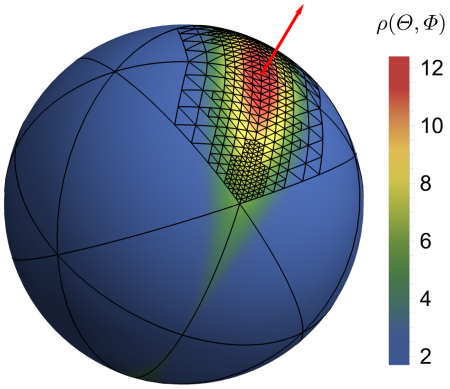

Figure 2: Illustrative discretization of a unit hemisphere with spherical triangles applied to a non-symmetric PDF of collagen fibers, represented by a bivariate von Mises distribution with the mean fiber direction **m** (red arrow). Image is taken from Rolf-Pissarczyk et al. [39].

The direction of a fiber in the reference configuration, denoted by the vector **N**, is given by

$$\mathbf{N}(\Theta,\Phi) = \sin\Theta\cos\Phi\mathbf{E}_1 + \sin\Theta\sin\Phi\mathbf{E}_2 + \cos\Theta\mathbf{E}_3, \tag{1}$$

where $\mathbf{E}_i$, $i = 1,2,3$, are the Cartesian unit basis vectors, while Θ and Φ are the polar and azimuth angles, respectively. We further define that the unit vector $\mathbf{N}(\Theta)$ lies on the unit hemisphere $\mathbb{S} = \{(\Theta,\Phi)|\Theta \in [0,\pi], \Phi \in [0,\pi]\}$. Because of symmetry, only half of the unit hemisphere needs to be considered. We then discretize the unit hemisphere into a finite number of elementary areas $\Delta\mathbb{S}_n$, $n = 1,\dots,m$, more precisely spherical triangles, as shown in Fig. 2.

By assuming a hyperelastic material, we now introduce the strain-energy function Ψ in a decoupled form as

$$\Psi = \Psi_{\text{vol}} + \Psi_{\text{iso}}, \tag{2}$$

where Ψ_{vol} and Ψ_{iso} represent the purely volumetric and isochoric parts. The volumetric part can be defined as

$$\Psi_{\text{vol}} = \frac{K}{4}(J^2 - 1 - 2\ln J), \tag{3}$$

and the isochoric part can be further decomposed into

$$\Psi_{\text{iso}} = \Psi_{\text{g}} + \Psi_{\text{c}}, \tag{4}$$

where Ψ_{g} represents the ground substance modeled by a neo-Hookean model and Ψ_{c} represents the energies stored in the collagen fibers.

To formulate the strain-energy function of collagen fibers in terms of the DFD method, we can write

$$\Psi_{\text{c}} = \sum_{i=4,6}\sum_{n=1}^{m}\rho_{cn}\Psi_{cn}(\bar{I}_{icn}), \tag{5}$$

where ρ_{cn} defines the discrete density of a fiber, $\Psi_{cn}(\bar{I}_{icn})$ is the single fiber strain energy represented by an exponential approach to model the stiffening of collagen fibers and $\bar{I}_{icn} = \bar{\mathbf{C}}\colon \mathbf{N}_n \otimes \mathbf{N}_n$ for two collagen fiber families i. The choice of (5) must ensure the condition $\Psi_n(1) = \Psi_n'(1) = 0$. After discretizing the unit hemisphere in m elementary areas, the discrete density ρ_{cn} of collagen fibers can be expressed as

$$\rho_{cn} = \frac{1}{2\pi}\int_{\Delta\mathbb{S}_n}\rho_{\text{c}}(\Theta,\Phi)\sin\Theta\,\text{d}\Theta\,\text{d}\Phi. \tag{6}$$

In addition, we must satisfy the normalization condition, which by definition is satisfied by the choice of the distribution function. For the discrete approach, i.e.

$$\sum_{n=1}^{m}\rho_{cn} = 1. \tag{7}$$

Then, to exclude compressed collagen fibers from the total strain-energy function, we distinguish the cases where f_{c} represents the mathematical expression of the strain-energy function of a single collagen fiber, while $I_{icn} = \mathbf{C}\colon \mathbf{N}_n \otimes \mathbf{N}_n$.

The isochoric part of the strain-energy function then reads

$$\Psi_{\text{iso}} = \Psi_{\text{g}}(\bar{I}_1) + \sum_{i=4,6}\sum_{n=1}^{m} \rho_{cn}\Psi_{cn}(\bar{I}_{icn}). \tag{8}$$

In order to implement the constitutive model framework in the open-source software SimVascular [54], the Cauchy stress tensor and the elasticity tensor need to be formulated. In this context, reference is made to previous studies [38, 39, 36].

We differentiate the isochoric strain-energy function (8) with respect to $\overline{\mathbf{C}}/2$ to identify the fictitious second Piola-Kirchhoff stress tensor $\overline{\mathbf{S}}$, i.e.

$$\overline{\mathbf{S}} = 2\frac{\partial \Psi_{\text{iso}}}{\partial \overline{\mathbf{C}}} = 2\psi'_{\text{g}}(\bar{I}_1)\mathbf{I} + 2\sum_{i=4,6}\sum_{n=1}^{m} \rho_{cn}\overline{\mathbf{S}}_{cn}(\bar{I}_{icn}), \tag{9}$$

where $\psi'_{\text{g}}(\bar{I}_{\text{g}}) = \partial\Psi_{\text{g}}(\bar{I}_1)/\partial\bar{I}_1$. The fictitious second Piola-Kirchhoff stress tensors for a single collagen fiber is denoted by $\overline{\mathbf{S}}_{cn}$. In analogy to Li et al. [27], we formulate

$$\overline{\mathbf{S}}_{cn} = \begin{cases} f'_{\text{c}}(\bar{I}_{icn})\mathbf{N}_n \otimes \mathbf{N}_n & \text{if} \quad I_{icn} \geq 1, \\ 0 & \text{if} \quad I_{icn} < 1, \end{cases} \tag{10}$$

where $f'_{\text{c}}(\bar{I}_{cn}) = \partial f_{\text{c}}(\bar{I}_{cn})/\partial\bar{I}_{cn}$. Applying the push-forward to (9) gives the fictitious Cauchy stress tensor $\overline{\boldsymbol{\sigma}}$. Hence,

$$\overline{\boldsymbol{\sigma}} = J^{-1}\overline{\mathbf{F}}\,\overline{\mathbf{S}}\,\overline{\mathbf{F}}^{\mathsf{T}} = 2J^{-1}\left(\psi'_{\text{g}}(\bar{I}_1)\bar{\mathbf{b}} + \sum_{i=4,6}\sum_{n=1}^{m} \rho_{cn}\overline{\boldsymbol{\sigma}}_{cn}(\bar{I}_{icn})\right), \tag{11}$$

with

$$\overline{\boldsymbol{\sigma}}_{cn} = \begin{cases} f'_{\text{c}}(\bar{I}_{icn})\mathbf{n}_n \otimes \mathbf{n}_n & \text{if} \quad I_{icn} \geq 1, \\ 0 & \text{if} \quad I_{icn} < 1, \end{cases} \tag{12}$$

where $\mathbf{n}_n = \mathbf{F}\mathbf{N}_n$. Next let us introduce the fourth-order projection tensor $\mathbb{p} = \mathbb{I} - \frac{1}{3}\mathbf{I} \otimes \mathbf{I}$ furnishing the physically correct deviator in the Eulerian description. Then, the double dot product of the projection tensor and the fictitious Cauchy stress tensor provides the isochoric Cauchy stress tensor, i.e.

$$\boldsymbol{\sigma}_{\text{iso}} = \mathbb{p} : \overline{\boldsymbol{\sigma}}, \tag{13}$$

where $\mathbb{I}$ denotes the symmetric fourth-order identity tensor, which can be represented by recalling the definition of the Kronecker delta δ_{ad} in component notation, i.e. $(\mathbb{I})_{abcd} = \frac{1}{2}(\delta_{ac}\delta_{bd} + \delta_{ad}\delta_{bc})$.

We formulate the fourth-order fictitious elasticity tensor $\overline{\mathbb{C}}$ in the Lagrangian description by differentiating the fictitious second Piola-Kirchhoff stress tensor $\overline{\mathbf{S}}$ with respect to $\overline{\mathbf{C}}/2$, and, subsequently, multiply it with the factor $J^{-4/3}$, so that we obtain

$$\overline{\mathbb{C}} = 2J^{-4/3}\frac{\partial \overline{\mathbf{S}}}{\partial \overline{\mathbf{C}}} = 4J^{-4/3}\left(\psi''_{\text{g}}(\bar{I}_1)\mathbf{I} \otimes \mathbf{I} + \sum_{i=4,6}\sum_{n=1}^{m} \rho_{cn}\overline{\mathbb{C}}_{cn}(\bar{I}_{icn})\right), \tag{14}$$

with

$$\overline{\mathbb{C}}_{\text{cn}} = \begin{cases} f''_{\text{c}}(\bar{I}_{icn})\mathbf{N}_n \otimes \mathbf{N}_n \otimes \mathbf{N}_n \otimes \mathbf{N}_n & \text{if} \quad I_{icn} \geq 1, \\ 0 & \text{if} \quad I_{icn} < 1, \end{cases} \tag{15}$$

where

$$\psi''_{\text{g}}(\bar{I}_1) = \frac{\partial^2 \Psi_{\text{g}}(\bar{I}_1)}{\partial\bar{I}_1\partial\bar{I}_1}, \qquad f''_{\text{c}}(\bar{I}_{icn}) = \frac{\partial^2 f_{\text{c}}(\bar{I}_{icn})}{\partial\bar{I}_{icn}\partial\bar{I}_{icn}}. \tag{16}$$

The fictitious elasticity tensor $\overline{\mathbb{c}}$ in the Eulerian description is then obtained by applying the push-forward to (14), which results in

$$\overline{\mathbb{c}} = 4J^{-1}\sum_{i=4,6}\sum_{n=1}^{m} \rho_{cn}\overline{\mathbb{c}}_{cn}(\bar{I}_{icn}) \tag{17}$$

with

$$\overline{\mathbb{C}}_{\text{cn}} = \begin{cases} f_c''(\bar{I}_{icn})\overline{\mathbf{n}}_n \otimes \overline{\mathbf{n}}_n \otimes \overline{\mathbf{n}}_n \otimes \overline{\mathbf{n}}_n & \text{if} \quad I_{icn} \geq 1 \\ 0 & \text{if} \quad I_{icn} < 1, \end{cases} \tag{18}$$

where $\overline{\mathbf{n}}_n = \overline{\mathbf{F}}\mathbf{N}_n$. Note that the term associated with the ground substance vanishes because the second derivative of the neo-Hookean model leads to $\psi_g''(\bar{I}_1) = 0$. Following on, the isochoric elasticity tensor $\mathbb{C}_{\text{iso}}$ is then obtained from (17), as defined in Holzapfel [20],

$$\mathbb{C}_{\text{iso}} = \mathbb{P} : \overline{\mathbb{C}} : \mathbb{P} + \frac{2}{3}\text{tr}(\overline{\boldsymbol{\sigma}})\mathbb{P} - \frac{2}{3}(\boldsymbol{\sigma}_{\text{iso}} \otimes \mathbf{I} + \mathbf{I} \otimes \boldsymbol{\sigma}_{\text{iso}}). \tag{19}$$

3.2 Implementation

SimVascular [54] is an open-source software that allows for the simulation of blood flow and cardiovascular systems. It is primarily used for cardiovascular research and education and is designed to work with image-based patient-specific models. The software allows for the creation of detailed three-dimensional models of blood vessels and the surrounding tissue, and it can be used to simulate blood flow and pressure, as well as to study the mechanics of cardiovascular disease and the effects of different treatment options. SimVascular is developed and maintained by a community of researchers, engineers, and clinicians, and it can be used in combination with other simulation tools.

The SimVascular [54] software was first developed in 2007 by Charles Taylor's lab at Stanford University. In 2013, the software was revitalized and advanced capabilities, such as discrete modeling and fluid-structure interaction modeling, were added to the source-code. The software offers a complete simulation pipeline for cardiovascular simulations, including medical image data segmentation, patient-specific blood flow simulation, and analysis. The software includes various solvers, such as svSolver, svZeroDsolver, svOneDsolver and svFSI, for solving different types of problems. Here, the author of this report used the svFSI solver to perform both structural and fluid-structure interaction problems.

One goal of this report is to implement an anisotropic material model, i.e. the introduced DFD method, see Section 3.1, into the existing Fortran source code. The implementation process involved incorporating the explicit second Piola-Kirchhoff stress tensor and the tangent in the reference configuration on a Gauss-point level, both were introduced before. The framework was designed to handle nearly incompressible cases, using a standard element formulation with a penalty term for the volumetric part. To ensure the accuracy and effectiveness of the model, various verification activities were carried out, including the use of representative examples. These activities helped confirm that the implemented model is suitable for use in larger computational studies, i.e. in FSI simulations, and the results of these activities are discussed in more detail in this report.

3.3 Verification

For the code verification, two representative numerical examples were generated to proof the correct implementation of the anisotropic material model (DFD method), i.e. simple tension and simple shear. The numerical solutions obtained with open-source software SimVascular [54] were here compared to an analytical solution.

Simple tension

In the present example, we consider a uniaxial extension test of an incompressible unit cube with the geometry $1 \times 1 \times 1\,\text{mm}$ composed of 32 tetrahedral elements, see Fig. 3(b).

The faces of the unit cube are aligned with the unit Cartesian basis vectors $\mathbf{E}_1, \mathbf{E}_2$ and $\mathbf{E}_3$. On the top face of the unit cube, we apply a displacement boundary condition. A rotational symmetric dispersion of two family of collagen fibers are assumed to demonstrate the performance of the proposed constitutive model. Due to symmetry, the deformation gradient for this problem is

$$[\mathbf{F}] = \text{diag}[\lambda^{-1/2}, \lambda^{-1/2}, \lambda], \tag{20}$$

where λ represents the stretch in the $\mathbf{E}_3$-direction. In analogy, for any fiber direction $\mathbf{N}$ within the half sphere, $I_{(\cdot)}(\mathbf{N})$ is given by

$$I_{(\cdot)}(\mathbf{N}) = \lambda^{-1}\sin^2\Theta + \lambda^2\cos^2\Theta, \quad (\cdot) = 4, 6. \tag{21}$$

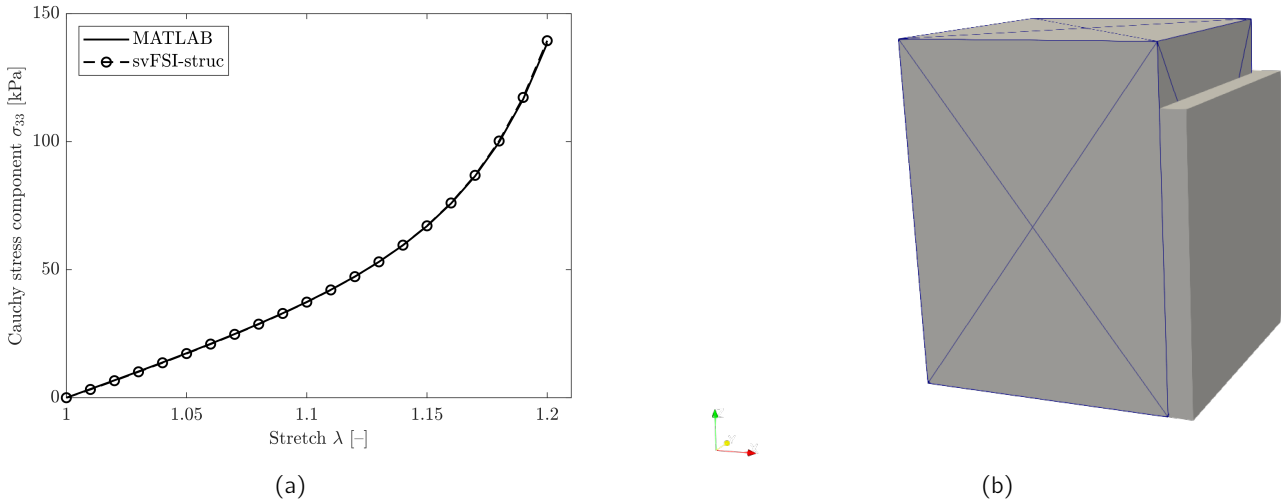

(a) (b)

Figure 3: (a) Comparison of the solutions of a uniaxial extension test obtained by using the continuous fiber dispersion method [26] in MATLAB and the finite element solutions obtained by using the isoparametric DFD method [39] in svFSI-struct with $m = 256$ discrete fiber directions. In this example, we applied a stretch of $\lambda = 1.2$ in the $\mathbf{E}_3$-direction. For both fiber families, the material parameters $\mu = 50\,\text{kPa}$, $k_1 = 8\,\text{kPa}$ and $k_2 = 12$, the value $b = 3$ of the concentration parameter, and the bulk modulus of $K = 2.5 \cdot 10^5$ was used [50]. (b) Reference and deformed configurations of a unit cube of rotationally symmetric dispersions of collagen fibers (mean fiber direction aligned with the loading direction).

Note that $I_{(\cdot)}(\mathbf{N})$ is independent of Φ for this particular case. Then, the Cauchy stress tensor $\boldsymbol{\sigma}$ over the integration domain $\Omega = \{(\Theta, \Phi) | \Theta \in [0, \pi/2], \Phi \in [0, 2\pi]\}$ of a half sphere, when the fiber dispersion is treated continuously, is

$$\boldsymbol{\sigma} = -p\mathbf{I} + \mu\mathbf{b} + \frac{k_1}{\pi}\int_\Omega \rho(\Theta,\Phi)\exp[k_2(I_4-1)^2] \times (I_4-1)\sin\Theta\mathbf{n}\otimes\mathbf{n}\mathrm{d}\Theta\mathrm{d}\Phi + \tag{22}$$

$$+ \frac{k_1}{\pi}\int_\Omega \rho(\Theta,\Phi)\exp[k_2(I_6-1)^2] \times (I_6-1)\sin\Theta\mathbf{n}\otimes\mathbf{n}\mathrm{d}\Theta\mathrm{d}\Phi \tag{23}$$

where p represents the Lagrange multiplier to ensure incompressibility. For this case, $\rho(\Theta, \Phi)$ reduces to

$$\rho(\Theta) = 4\sqrt{\frac{b}{2\pi}}\frac{\exp\left(2b\cos^2\Theta\right)}{\text{erfi}(\sqrt{2b}\,)}. \tag{24}$$

Following Li et al. [28], the uniaxial Cauchy stress $\sigma \equiv \sigma_{33}$ in the $\mathbf{E}_3$-direction is expressed by

$$\sigma = (\mu + \alpha_4 + \alpha_6)\lambda^2 - (\mu + \beta_4 + \beta_6)\lambda^{-1}, \tag{25}$$

where $\alpha_{(\cdot)}$ and $\beta_{(\cdot)}$ are defined over the domain $\Sigma = \{\Theta \in [0, \pi/2]\}$ as

$$\alpha_{(\cdot)} = 2k_1\int_\Sigma \rho(\theta)\exp[k_2(I_{(\cdot)}-1)^2](I_{(\cdot)}-1)\sin\Theta\cos^2\Theta\mathrm{d}\Theta, \tag{26}$$

$$\beta_{(\cdot)} = k_1\int_\Sigma \rho(\theta)\exp[k_2(I_{(\cdot)}-1)^2](I_{(\cdot)}-1)\sin^3\Theta\mathrm{d}\Theta. \tag{27}$$

The numerical integrations of the coefficients $\alpha_{(\cdot)}$ and $\beta_{(\cdot)}$ were evaluated in MATLAB with the built-in function *quadgk* using the adaptive Gauss-Kronrod quadrature method to verify the finite element solution of this problem by using the DFD model, see Li et al. [26].

The Cauchy stress versus stretch result was implemented in MATLAB, and we obtained solutions of this problem with material parameters $\mu = 100\,\text{kPa}$, $k_1 = 8\,\text{kPa}$ and $k_2 = 12$ for both fiber families, the value $b = 3$ of the concentration parameter, and the bulk modulus of $K = 2.5 \cdot 10^5$ [50]. The relationship between the Cauchy stress and the stretch in the loading direction is shown in Fig. 3(a). For comparison, we have plotted the finite element solutions (open circles) by using the isoparametric DFD model in svFSI-struct with $m = 256$ discrete fiber directions, which is enough to obtain very accurate results. As can be seen in Fig. 3(a), a very good match between the MATLAB and the finite element solution has been obtained.

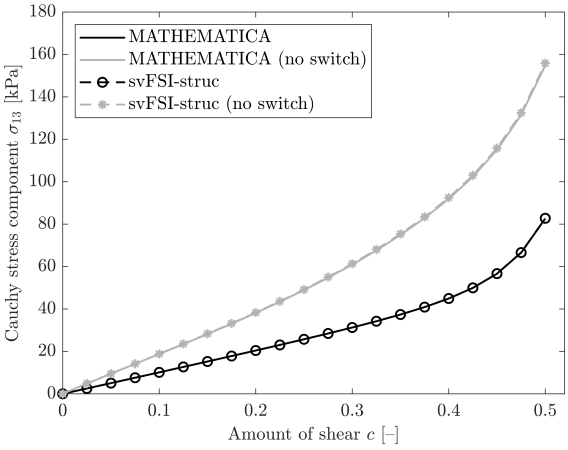

(a)

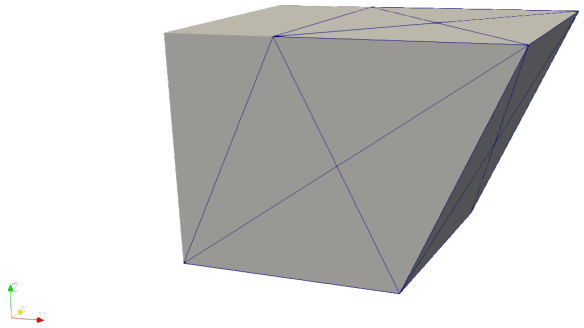

(b)

Figure 4: (a) Comparison of the solutions of a simple shear test obtained by using the continuous fiber dispersion method [26] in MATHEMATICA and the finite element solutions obtained by the isoparametric DFD method [39] in svFSI-struct with $m = 256$ discrte fiber directions. In this example, we applied an amount of shear of $c = 0.5$ (with and without tension-compression switch of collagen fibers). For both fiber families, the material parameters are $\mu = 100\,\text{kPa}$, $k_1 = 80\,\text{kPa}$ and $k_2 = 12$, the value $b = 3$ of the concentration parameter, and the bulk modulus of $K = 2.5 \cdot 10^7$ [50]. (b) Deformation of a unit cube under simple shear in the ($\mathbf{E}_1$, $\mathbf{E}_3$)-plane. The mean fiber direction is aligned at 135° clockwise from the $\mathbf{E}_3$ direction in the reference configuration (in the ($\mathbf{E}_1$, $\mathbf{E}_3$)-plane).

Simple shear

In this example, we apply a simple shear deformation to an incompressible unit cube in the $(\mathbf{E}_1, \mathbf{E}_3)$-plane with the geometry of $1 \times 1 \times 1\,\text{mm}$, which is discretized by 32 tetrahedral elements, as illustrated in Fig. 4(b).

Boundary conditions are chosen such that all the nodes on the $(\mathbf{E}_1, \mathbf{E}_2)$-plane are constrained in all three translational degrees of freedom, and on the top face of the unit cube a horizontal displacement in the $\mathbf{E}_1$-direction is applied. Thus, for this particular case, we can formulate the deformation gradient in the matrix form as

$$[\mathbf{F}] = \begin{bmatrix} 1 & 0 & c \\ 0 & 1 & 0 \\ 0 & 0 & 1 \end{bmatrix}, \tag{28}$$

where c represents the amount of shear, and $I_{(\cdot)}(\mathbf{N})$ is given in the explicit by

$$I_{(\cdot)}(\Theta, \Phi) = 1 + c^2 \cos^2\Theta + c \sin 2\Theta \cos\Phi. \tag{29}$$

In analogy to Li et al. [28], the Cauchy shear stress component σ_{13} in the $(\mathbf{E}_1, \mathbf{E}_2)$-plane is given by

$$\sigma_{13} = (\mu + \alpha_4 + \alpha_6)c + \gamma_4 + \gamma_6, \tag{30}$$

where the factors $\alpha_{(\cdot)}$ and $\beta_{(\cdot)}$ are defined over the domain $\Omega = \{(\Theta, \Phi) \in \mathbb{S} | I_{(\cdot)} > 1\}$ as

$$\alpha_{(\cdot)} = \frac{k_1}{\pi} \int_\Omega \rho(\Theta, \Phi)(I_{(\cdot)} - 1)\exp[k_2(I_{(\cdot)} - 1)^2] \sin\Theta \cos^2\Theta \mathrm{d}\Theta\mathrm{d}\Phi, \tag{31}$$

$$\gamma_{(\cdot)} = \frac{k_1}{\pi} \int_\Omega \rho(\Theta, \Phi)(I_{(\cdot)} - 1)\exp[k_2(I_{(\cdot)} - 1)^2] \sin^2\Theta \cos\Theta \cos\Phi \mathrm{d}\Theta\mathrm{d}\Phi. \tag{32}$$

We implemented the result in MATHEMATICA and obtained the solution for σ_{13} as a function of the amount of shear. For this problem, for two families of collagen fibers, we used the material parameters $\mu = 100\,\text{kPa}$, $k_1 = 80\,\text{kPa}$ and $k_2 = 12$, the value $b = 3$ of the concentration parameter, and the bulk modulus of $K = 2.5 \cdot 10^7$ [50]. As can be seen, the numerical results match very well with the corresponding analytical results from Li et al. [26].

4 A patient-specific FSI model of aortic dissection

The patient-specific FSI framework is explained in the next section. It starts by providing an overview of the patient data, then explains the model and mesh generation process and the governing equations used in the

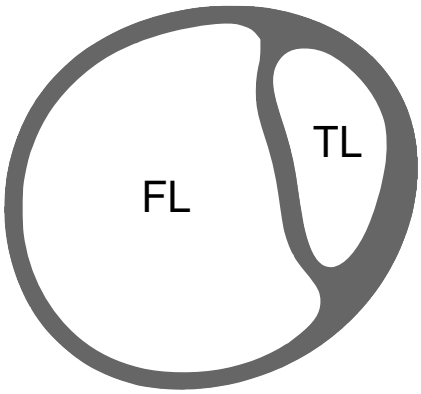

Figure 5: Cross-section of the patient-specific type B aortic dissection with varying wall thicknesses for the outer wall true lumen (TL), for the dissection flap and for the outer wall false lumen (FL).

arbitrary lagrangian eulerian (ALE) framework. Lastly, the numerical framework for the FSI simulation is outlined, including information on boundary conditions, the creation of a local coordinate system, material parameters, and the method for calculating prestresses in the aortic wall.

4.1 Patient data

A three-dimensional computed tomography angiography imaging data of a type B aortic dissection case from a 28-year-old female before receiving a graft was selected from the institutional database of Prof. Dominik Fleischmann. The imaging protocol followed relevant regulations and was approved by the institutional review board of Stanford University. Written informed consent was obtained before the computed tomography angiography acquisition. The type B aortic dissection case showed a tear in the proximal area near the left subclavian artery and another tear in the distal area above the celiac trunk. The approximate size of the entry tear in a double oblique plane was $228\,\mathrm{mm}^2$ and the size of the exit tear was $227\,\mathrm{mm}^2$. No other vessels, except for intercostal arteries, were found branching off of the true lumen or false lumen.

4.2 Model generation

We segmented the patient-specific anatomic model using computed tomography angiography images taken during mid-diastole. The model includes the following branch vessels: the brachiocephalic trunk, the left common carotid, and the left subclavian artery in the aortic arch, the celiac artery, the superior mesenteric artery, and the renal arteries in the abdomen, as well as the internal and external iliac arteries. The image segmentation and model generation were performed using SimVascular [54], the open-source patient-specific cardiovascular flow modeling software. Additional editing was done using Meshmixer (Autodesk, Inc.).

The FSI simulation requires two separate meshes: One for the fluid domain and a second for the structural domain, which includes the vessel wall and dissection flap. We have designed a special procedure to ensure that the outer wall of the fluid domain aligns with the inner wall of the structural domain. The modeling pipeline includes the following steps:

1. Fluid domain segmentation: We began by creating two separate surface models: One for the true lumen and another "combined" model, which included the outer arterial wall (adventitial layer), the true lumen, and the dissection flap. Using Meshmixer, we then created an additional model, called the "extruded true lumen model," by extending the true lumen model. By subtracting the extruded model from the combined model using Boolean operations, we obtained the false lumen model. By merging the initial true lumen model with this false lumen model, and performing local smoothing operations, we created a model of the fluid domain. The previous extrusion of the true lumen model resulted in a uniform dissection flap separating the true and false lumen.

2. Solid domain segmentation: To obtain the solid domain model (the model of the vessel wall and the dissection flap), we first outwardly extruded the individual domains by a uniform parameter h_{wall}, which defines the outer wall thickness (Fig. 5). To be more specific, a wall thickness for the outer wall true lumen, the dissection flap, the outer wall false lumen and the branch vessels was defined, which were based on measurements on dissected tissue performed in our laboratory (Institute of Biomechanics, Graz University of Technology,

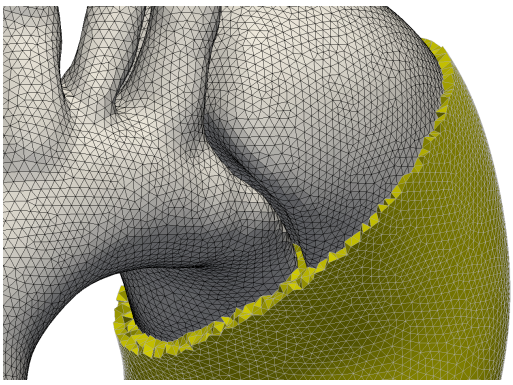

Figure 6: An image of the patient-specific geometry meshed with tetrahedral elements is presented. The fluid domain was approximatively meshed with 1 million finite elements and the solid domain with 0.33 million finite elements.

Austria, Graz). The Boolean difference between this extruded model and the fluid domain model, again followed by local smoothing operations, resulted in the structural domain model. These values are within the reported range average adult arterial wall thickness [40, 34].

4.3 Mesh generation

For the geometric model, we created unstructured tetrahedral meshes for the fluid and structural domains using the TetGen mesh generator [49], which is integrated in open-source software SimVascular [54]. The fluid mesh consisted of approximately 1 million finite elements and the solid domain was meshed with 0.33 million finite elements. The fluid and structural meshes were designed so that the nodes at the interface between the two domains coincide, which eliminates the need for additional numerical treatments to handle the interface constraints that are detailed later. More information about the mesh generation process can be found at the given reference: http://simvascular.github.io/docssvFSI.html.

4.4 Governing equations

The blood flow in the patient-specific model is modeled as an incompressible, Newtonian fluid, which is a common assumption for larger arteries [55]. The Navier-Stokes equations, in ALE formulation, are used to govern the fluid flow

$$\varrho_f \hat{\partial}_t \mathbf{v} + \varrho((\mathbf{v} - \hat{\mathbf{v}}) \cdot \nabla)\mathbf{v} - \operatorname{div} \boldsymbol{\sigma}_f = 0 \quad \text{in } \Omega_f(t) \tag{33}$$

$$\operatorname{div} \mathbf{v} = 0 \quad \text{in } \Omega_f(t), \tag{34}$$

taking into account the deformability of the fluid domain $\Omega_f(t)$ via the grid velocity $\hat{\mathbf{v}}$ and via the ALE time derivative $\hat{\partial}_t$. The Cauchy stress tensor for the blood, which is assumed to be a Newtonian fluid, is represented by $\boldsymbol{\sigma}_f$. It is given as $\boldsymbol{\sigma}_f = \mu_f(\nabla\mathbf{v} + \nabla\mathbf{v}^{\mathsf{T}}) - p\mathbb{I}$, where $\mathbf{v}$ is the fluid velocity and p is the pressure. The gradient operator ∇ is used for spatial derivatives in the Eulerian frame and $\mathbb{I}$ is the identity tensor. The fluid density and viscosity are represented by ϱ_f and μ_f, respectively, and have been assigned the values of $1060\,\mathrm{kg/m^3}$ and $0.004\,\mathrm{Pa\,s}$.

The arterial wall is modeled as a homogeneous, anisotropic, and nonlinear material using the constitutive framework in Section 3.1. A mapping linking the coordinates in the current domain $\mathbf{x}$ at time t to the material coordinates in the reference configuration $\mathbf{X}$ is defined through the displacement field $\mathbf{u}$, as

$$\mathbf{x}(X, t) = X + \mathbf{u}(X, t), \tag{35}$$

The reference configuration is chosen to be the same as the initial configuration. The governing equation in the reference domain Ω_s is given by

$$\varrho_s \partial_{tt}\mathbf{u} + \operatorname{div}_X(\mathbf{FS}) = 0 \quad \text{in } \Omega_s, \tag{36}$$

where ϱ_s is the structural density, $\mathbf{F}$ is the deformation gradient tensor, and $\mathbf{S}$ is the second Piola–Kirchhoff stress tensor. External forces such as gravity are neglected, and the reference domain is independent of time t.

4.5 Numerical framework

The numerical simulations are carried out using the svFSI finite element solver from the open-source software SimVascular [54], which utilizes linear elements for velocity and pressure. The finite element spaces are stabilized with weighted residuals, using the residual-based variational multiscale method (RBVMS). This technique acts as a stabilization for the $\mathcal{P}1/\mathcal{P}1$ finite element space, which otherwise does not fulfill the Ladyzhenskaya–Babuška–Brezzi (LBB) stability condition, and also in the strong advective regime. The RBVMS has been previously validated in a variety of cardiovascular simulations [12, 53]. For more information, the reader can refer to the references provided [3, 4, 52, 13]. The fluid and structural domain are solved as a strongly coupled linear system using the monolithic approach. Backflow stabilization is applied at the fluid outlets as described in previous studies [12].

Fluid domain boundary conditions

At the inlet, we prescribe a time-dependent Dirichlet condition with a given velocity $\mathbf{v}_{in}$. The inlet flow rate is obtained from the patient-specific inflow profil, see [60]. Nodal values at the inlet face are then prescribed by assuming a parabolic cross-sectional flow profile. In cardiovascular simulations, it is important to choose appropriate outlet boundary conditions that incorporate downstream vasculature effects into the three-dimensional simulation, such as vessel wall impedance and wave propagation. We prescribe three-element Windkessel boundary conditions, according to the coupled multidomain method as described in [12]. Details of the tuning procedure to identify the Windkessel parameters are given later.

Prestress

The arterial wall is constantly subjected to mechanical forces such as blood pressure and viscous forces. To accurately simulate these conditions, our numerical methodology takes into account the initial loading state of the anatomic model derived from computed tomography angiography data, which is in equilibrium with hemodynamic conditions at diastole.

Two main approaches have been reported for this purpose. The first approach involves determining an initial zero-stress geometry by deflating the model [53, 51], so that when the model is subsequently subjected to hemodynamic equilibrium conditions, the inflated model matches the original segmentation. The second approach, proposed by Hsu and Bazilevs [22], involves determining a prestress tensor, which allows for the vessel deformation to correspond to the segmentation derived from the imaging data when the prestressed vessel is subjected to hemodynamic equilibrium conditions. In this report, we adopt the second approach, which includes determining a prestress tensor and subsequently applying it to the model. It consists of the following steps, which are described in Bäumler et al.[2]:

1. To begin, an approximation of the traction $\mathbf{h}$ on the aortic walls during diastole is obtained by conducting a simplified CFD simulation. This simulation considers rigid walls and a constant inflow rate, and the outlets are set as resistance boundary conditions to achieve a steady state that corresponds to the patient's diastolic pressure and flow. Once the steady state of velocity $\mathbf{v}$ and pressure p is achieved, the traction vector $\mathbf{h} = \boldsymbol{\sigma}(\mathbf{v}, p)\mathbf{n}$ is calculated on the outer wall of the fluid domain.

2. In the second step of the numerical methodology, we aim to identify a prestress tensor $\mathbf{S}_0$ in the arterial wall that satisfies the momentum balance between the structure's internal stresses and fluid traction for all vector-valued test functions w,

$$(\nabla_x w, \mathbf{F}\mathbf{S}_0)_{\Omega_s} + (w, \mathbf{h})_{\Gamma(t=0)} = 0. \tag{37}$$

   This equation generates multiple possible solutions for $\mathbf{S}_0$ and we use an iterative method to identify a specific solution. The process starts by initializing $n = 0$ and $\mathbf{S}_0^n = \mathbf{0}$. Then, we repeat steps (a) to (c) until we find a solution.

   (a) Set $\mathbf{S}_0 = \mathbf{S}_0^n$ and $\mathbf{u} = 0$. This also sets $\mathbf{F} = \mathbb{I}$ and $\mathbf{S} = 0$.

   (b) Find $\mathbf{u}$ such that for all vector-valued test functions the variational formulation

$$(w, \varrho_s \partial_{tt}\mathbf{u})_{\Omega_s} + (\nabla_X w, \mathbf{F}(\mathbf{S} + \mathbf{S}_0))_{\Omega_s} + (w, \mathbf{h})_{\Gamma(t=0)} = 0 \tag{38}$$

   is satisfied. Here, the previously determined traction vector $\mathbf{h}$ is applied as the boundary condition at the fluid–structure interface Γ.

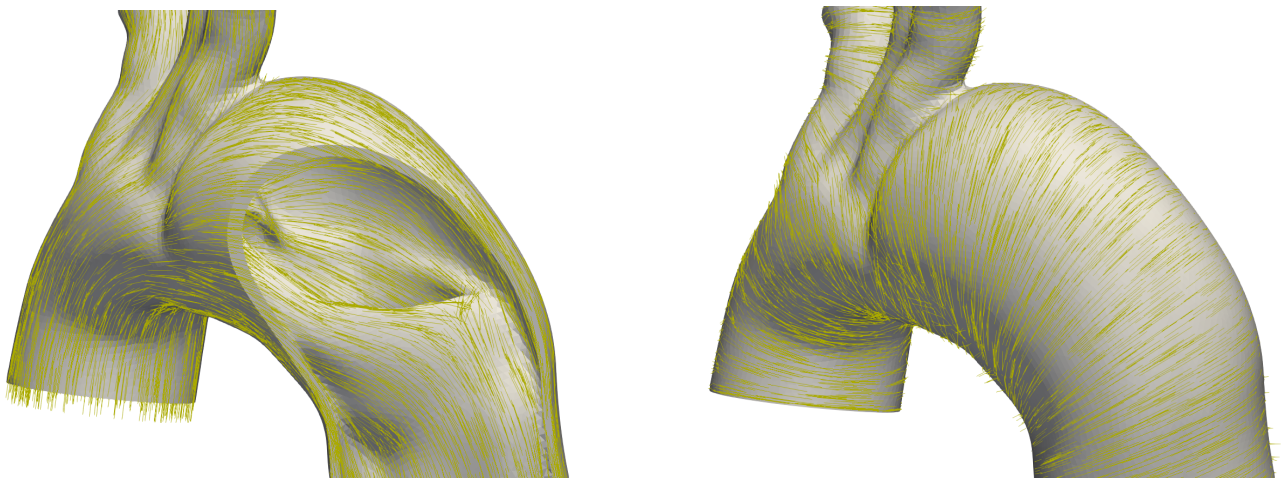

(a) (b)

Figure 7: An image of the patient-specific geometry with the local fiber direction in (a) longitudinal direction and (b) circumferential direction.

(c) Update $\mathbf{S}_0^{n+1} = \mathbf{S} + \mathbf{S}_0^n$, increment n by $n = n + 1$.
The iterations are stopped once an equilibrium is established and the aortic wall, subject to prestress and prescribed traction, yields zero displacement $\mathbf{u} = 0$, $\mathbf{F} = \mathbb{I}$, and $\mathbf{S} = 0$. Consequently, the solution $\mathbf{S}_0$ satisfies Eq. (37).

3. After the prestress tensor $\mathbf{S}_0$ is determined, we perform two-way FSI simulations by augmenting the stress tensor with $\mathbf{S}_0$:

$$\varrho_s \partial_{tt}\mathbf{u} + \operatorname{div}_X(\mathbf{F}(\mathbf{S} + \mathbf{S}_0)) = 0 \quad \text{in } \Omega_s(t) \tag{39}$$

Under diastolic flow conditions, augmented by the prestress tensor, the prestressed arterial wall maintains the shape extracted from the computed tomography angiography scan.

The method outlined above, which involves determining an initial zero-stress geometry by deflating the model and then applying a prestress tensor to it, was first proposed by Hsu and Bazilevs [22] for geometries with an intact arterial wall. However, in the case of a dissection flap, the pressure differential is much smaller, and the flap remains relatively still during diastole. Therefore, it is assumed that the dissection flap is not prestressed during diastole in vivo, and the prestress tensor $\mathbf{S}_0$ is only applied to the outer arterial wall in the final step of the algorithm.

Local fiber direction

Creating a material orientation for the patient-specific model used in the report (see Fig. 7) that accurately represents the local physiology of complex solid shapes is challenging, as described by Schussnig et al. [45]. To overcome this, various computational methods are used that are designed to be fast, reliable and easy to adjust by the user. These methods often involve solving multiple Laplace problems with user-specified boundary data, which can be applied to a vessel network and can be formulated as

$$-\Delta\phi_l = 0 \quad \text{in } \hat{\Omega}_s, \tag{40}$$

$$\phi_l = 0 \quad \text{on } \hat{\Gamma}_{in,s}, \tag{41}$$

$$\hat{\mathbf{n}}_s \cdot \nabla\phi_l = h_{l,i} \quad \text{on } \hat{\Gamma}_{i,s},\ i = 1, \ldots, N_{out}, \tag{42}$$

$$\hat{\mathbf{n}}_s \cdot \nabla\phi_l = 0 \quad \text{on } \hat{\Sigma} \cup \hat{\Gamma}_{R,s}, \tag{43}$$

where the auxiliary scalar ϕ_l for the longitudinal orientation is prescribed at the inlet face of the solid $\hat{\Gamma}_{in,s}$, normal fluxes $h_{l,i}$ are prescribed at the solid outlet faces $\hat{\Gamma}_{i,s}$, $i = 1, \ldots, N_{out}$ and zero fluxes are enforced at the interface and exterior boundary. The $h_{l,i}$ are tuned to yield ϕ_l with a large enough gradient, such that

$$\mathbf{e}_2 := \frac{\nabla\phi_l}{||\nabla\phi_l||} \tag{44}$$

approximates the longitudinal direction $\mathbf{e}_2$ reasonably well. In a similar manner, a scalar ϕ_n to approximate the tissue-normal direction can be constructed via

$$-\Delta\phi_n = 0 \quad \text{in } \hat{\Omega}_s, \tag{45}$$

$$\phi_n = 0 \quad \text{on } \hat{\Sigma}, \tag{46}$$

$$\hat{\mathbf{n}}_s \cdot \nabla\phi_n = 0 \quad \text{on } \hat{\Gamma}_{in,s} \cup \hat{\Gamma}_{i,s},\ i = 1, \ldots, N_{out}, \tag{47}$$

$$\hat{\mathbf{n}}_s \cdot \nabla\phi_n = h_n \quad \text{on } \hat{\Gamma}_{R,s}, \tag{48}$$

setting appropriate values h_n to achieve a reasonable tissue-normal direction $\mathbf{e}_3 := \nabla\phi_n / ||\nabla\phi_n||$. The rule-based assignment of boundary conditions and tuning parameters, while effective for handling complex geometries such as curved, bulging, or bifurcating vessels, is not well-suited for changes that are confined to the cross-section of the vessel alone. A prime example of this is found in aortic dissection, where the original lumen splits into distinct true and false lumina, as seen in references such as [48, 35, 10]. In this scenario, identifying the tissue layer separating these lumina and assigning proper boundary conditions, or even dividing the problem into multiple subproblems, is necessary to achieve accurate material orientation throughout the dissected vessel. However, this approach may require additional tuning parameters or manual markers, making it less practical for clinical applications.

The algorithm utilizes a method of extrapolating the averaged normal vector on the fluid-structure interface into the structural domain to approximate the tissue normal direction. This approach is effective even in areas where the fluid is in contact with the tissue from both sides. The first step in the process is to determine the normal vectors $\hat{\mathbf{n}}_s$ on the fluid-structure interface $\hat{\Sigma}$ for all elements that lie on it. Next, the mean orientations of all elements that are in contact with the previously marked element layer are determined, taking into consideration the neighbors of each element. This second step is repeated until the interface normal, which will later be used as $\mathbf{e}_3$, is set in all elements. It is important to consider either only data from the first neighbor of each element that has an orientation, or, as an alternative, to consider all neighbors of a given element that have a radial direction $\mathbf{e}_{3,j}$ deviating from the first encountered neighbor with orientation $\mathbf{e}_{3,i}$ that satisfies the following equation:

$$\alpha_{tol} \geq \arccos\left(\frac{\mathbf{e}_{3,i} \cdot \mathbf{e}_{3,j}}{||\mathbf{e}_{3,i}||\,||\mathbf{e}_{3,i}||}\right). \tag{49}$$

This algorithm incorporates the normal direction $\mathbf{e}_{3,j}$ from a neighboring element j only if the angle between $\mathbf{e}_{3,j}$ and $\mathbf{e}_{3,i}$ from the first encountered neighbor deviates less than a tolerance angle α_{tol}. This is done by repeating a few conditional averaging cycles in order to obtain a satisfactory vector field. It is important to note that the tissue circumferential direction $\mathbf{e}_1$, which is constructed from the normal $\mathbf{e}_3$ and longitudinal directions $\mathbf{e}_2$, may be inverted. Therefore, this method is only applicable when the tissue's response does not change when inverting the circumferential direction $\mathbf{e}_1$, which is the case for symmetric fiber reinforcements typically used in the cardiovascular context.

The extrapolation of $\hat{\mathbf{n}}_s$ into $\hat{\Omega}_s$ is then directly used as the tissue-normal direction $\mathbf{e}_3$, while the step to generate the longitudinal orientation $\mathbf{e}_2$ remains unchanged (see, e.g., [46, 43, 42]). Based on the normalised longitudinal direction $\mathbf{e}_2$ and normal direction $\mathbf{e}_3$, the circumferential direction is defined as

$$\mathbf{e}_1 := \frac{\mathbf{e}_2 \times \mathbf{e}_3}{||\mathbf{e}_2 \times \mathbf{e}_3||} \tag{50}$$

The mean fiber directions $\mathbf{m}_i$, symmetrically inclined by some angle α_c from circumferential to longitudinal direction, are then conveniently constructed via

$$\mathbf{m}_4 := \frac{\mathbf{e}_1 + \mathbf{e}_2 \tan(\alpha_c)}{||\mathbf{e}_1 + \mathbf{e}_2 \tan(\alpha_c)||}, \quad \mathbf{m}_6 := \frac{\mathbf{e}_2 + \mathbf{e}_2 \tan(-\alpha_c)}{||\mathbf{e}_1 + \mathbf{e}_2 \tan(-\alpha_c)||} \tag{51}$$

These mean fiber directions $\mathbf{m}_i$, $i = 4, 6$ are then needed for the definition of the PDFs, as introduced in Section 3.1. The overall approach construct physiologically meaningful material orientation vectors $\mathbf{e}_1$ and $\mathbf{e}_2$ with extrapolated interface normal and conditional averaging is summarised in the Algorithm shown in the study of Schussnig et al. [45].

For vessels with a curved centreline, bifurcations or even aneurysms, material orientations based on two Laplace problems with suitable boundary conditions can yield satisfactory results as, e.g., shown in our previous work [44] for an idealised abdominal aortic aneurysm.

Solving another Laplace equation requires not only a subdivision into regions, but also detecting a specific side of the dissection flap. As spatial discretisations of such cases can lead to rather smooth transitions in the flap's surface mesh more involved techniques or even manual intervention are necessary here. Thus, assigning appropriate boundary conditions is non-trivial. Such an approach is indeed applicable for obtaining a material orientation in

the aortic wall; however, in the flap region (wetted from both sides), the constructed $\mathbf{e}_1$ does not even remotely approximate the expected circumferential direction. A suitable orientation can be constructed by using an Algorithm shown by Schussnig et al. [45] with $\alpha_{tol} = 120°$ for conditional averaging and $N_{avg} = 5$ cycles of averaging after initial extrapolation of the interface normal. Inspecting the vector fields, substantial improvements are obvious.

Structural domain boundary condition

At each ring-shaped outlet of the structural domain, we prescribe homogeneous Dirichlet boundary conditions, $\mathbf{u} = 0$, to fix the outlets in place. Additional treatment is necessary to apply boundary conditions on the outer arterial wall. The aorta is surrounded by various tissues and organs which restrict its movement and dilation. To account for this, we apply an external tissue support as described below. As a result, we choose a Robin-type boundary condition,

$$\boldsymbol{\sigma}_s \mathbf{n} = -k_s \mathbf{u} - c_s \partial_t \mathbf{u} - p_0 \mathbf{n}, \tag{52}$$

which has been used to account for viscoelastic tissue support on the outer arterial wall [30, 29, 37]. The user-chosen parameters k_s and c_s model the viscoelastic response of the external tissue and p_0 the external pressure in the thoracic and abdominal cavities. We prescribe a nonzero value $k_s = 1 \cdot 10^7 \frac{Ns}{m^3}$ and set $p_0 = c_s = 0$, which is within the range of parameters reported in the literature and accounts for tethering of the external wall. Simulation results with and without external tissue support ($k_s = 0 \frac{Ns}{m^3}$ and $k_s = 1 \cdot 10^7 \frac{Ns}{m^3}$).

Interface

At the interface $\Gamma(t)$ between the fluid and structural domain, the kinematic and dynamic boundary condition needs to be fulfilled, given as

$$\mathbf{v} = \partial_t \mathbf{u} \quad \text{on } \Gamma(t) \tag{53}$$

$$\boldsymbol{\sigma}_f \mathbf{n}_f + \boldsymbol{\sigma}_s \mathbf{n} = 0 \quad \text{on } \Gamma(t). \tag{54}$$

Both equations are automatically fulfilled in our numerical method, since we enforce a nodal correspondence of velocity and pressure values at the fluid–structure interface during model creation.

Material parameters

The material properties for the simulation are based on biaxial extension tests on dissected tissue, which were perform in our laboratory. We defined for the specific domains, i.e. the outer wall true lumen, the dissection flap and the outer wall false lumen, specific material parameters. For comparison, in a healthy aorta, the elastic modulus is reported to be in the range of 200–800 kPa [32]. Literature data for the elastic modulus of the dissection flap tissue is not available. Arterial tissue is generally considered incompressible [17]. However, in the current framework we model the tissue as nearly incompressible by setting the Poisson ratio $\nu = 0.49$ in the whole structural domain.

Tuning of Windkessel parameters

Once the prestress tensor $\mathbf{S}_0$ is determined, we manually tune the three-element Windkessel parameters to match patient-specific pressure (125/75 mmHg). Tuning is considered successful when the systolic blood pressure P_{sys}, the diastolic blood pressure P_{dia}, the mean blood pressure $P_{mean} = \frac{1}{3}(P_{sys} + 2P_{dia})$, as well as the pressure amplitude are met within a tolerance of 10 %. To reduce computational cost, we perform an initial tuning procedure on a coarse mesh. Once the initial tuning is successful, we fine-tune the parameters on the fine mesh.

The total resistance R_T and capacitance C_T are distributed proportional to the flow at each outlet i: $R_{T,i} = R_T / q_i$ and $C_i = C_T \cdot q_i$. This distribution yields an approximation to the flow splits. The distal and proximal resistance at each outlet is then given by $R_{d,i} = k_d R_{T,i}$, and $R_{p,i} = (1 - k_d) R_{T,i}$, where the factor k_d defines the ratio of distal to total resistance in our three-element Windkessel model, and was fixed for all outlets to $k_d = 0.9$ [25, 24].

Discretization

To determine the necessary spatial resolution, we ran a sequence of simulations on successively refined meshes with uniform edge sizes. The final mesh of the full model consisted of approximately 1.3 million tetrahedral elements. The temporal resolution was set to 4000 timesteps per cardiac cycle, with a cycle length of 0.78 s, corresponding to a time step size of 0.195 ms. We used an iterative GMRES linear solver with a resistance preconditioner as described

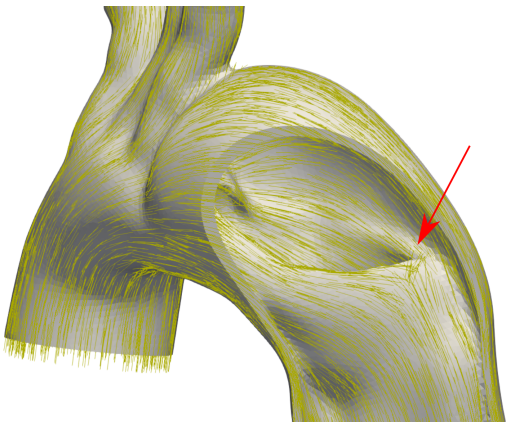

Figure 8: An image of the patient-specific geometry with the local fiber direction in longitudinal direction, where the red arrow shows the area of incorrect local fiber directions.

in Esmaily-Moghadam et al [13] and Seo et al. [47]. With the final setup, one cardiac cycle runs for approximately 9 h on 336 cores on Intel Xeon Platinum 8160 ('Skylake') compute nodes. Depending on the configuration of the simulation, cycle-to-cycle periodicity is usually achieved within 3 to 5 cycles. To report simulation results, we evaluate the results from the last cardiac cycle.

4.6 Preliminary results and problems encountered

We successfully performed FSI simulations with an isotropic material model of the aortic wall. This model does not incorporate the anisotropic material response of the aortic wall and hence also does not require a local fiber direction. The material model is only describe by isotropic part of the material model introduced in Section 3.1, i.e. only a single material parameter, the shear modulus μ, describes the material behavior. However, only preliminary results are available until now, because we did not complete the post-processing within the time frame of the research stay. The post-processed result will be obtained in the following weeks and months and will be published in a original paper. In the following, specific numerical problems that have arisen will be discussed.

The simulations with the anisotropic material model did not converge at this point. We observed several problems in the numericeal model that might have led to the convergence problems. First, as reported in previous study, the local fiber orientation shows local inconsistencies. For example, as shown in Fig. 8, the local coordinate system proximal to the intimal tear is incorrect. This can be laid back to the numerical approach used. Here, we set up a heat-transfer problem, which is described within the scope of this report, to compute the local fiber orientation. The nature of this approach causes the local fiber orientation to go around the intimal tear. At this point, is it not clear how to the change it, but other studies showed that it can still produce reasonable results.

A second problem are stress concentrations in some regions, which led to the abortion of simulations. They were observed at the intimal tear (as shown in Fig. 9) and in between two domains, e.g., between the outer wall of the false lumen and the dissection flap. Here, the material parameters changes suddenly. To circumvent this problem, we will investigate on different solutions. One solution could be to use a finer finite element mesh. A finer mesh could increase the quality of the finite elements, which subsequently leads to improved convergence. Another solution could be to implement different numerical damping methods in the finite element code. This solution could reduce the effect of oscillations in the numerical solution. Finally, another reason could be that the convergence is too sensitive to the choice of material parameters. It is known that specific sets of material parameter, in particular related to the anisotropic part led to a badly converging solution. Hence, different sets of material parameters need to be investigated.

Another problem to mention here is the high computational time of the anisotropic material model, which was presented in Section 3.1. It takes up to 10 times longer than a simple isotropic, material model like the neo-Hookean material model. Efforts have already been made to make the model more efficient, with success. However, it is still significantly slower than other approaches, such as the Holzapfel-Gasser-Ogden model, which is already implemented in SimVascular.

5 Discussion

In this report, we provided an overall overview about this project with the necessary background information. Then, we detailed the constitutive framework of the anisotropic model that was subsequently implemented in the

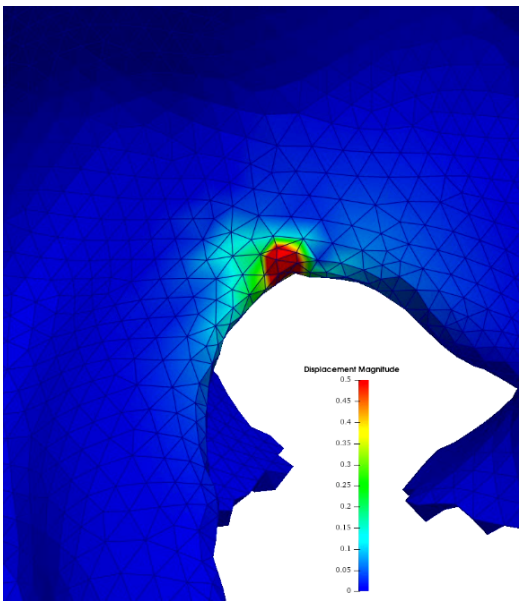

Figure 9: A picture showing the area of large displacements near the intimal flap. In general, large displacement can often be are related to high stresses.

open-source software SimVascular [54]. For this, representative numerical examples were shown to show that the implementation was correctly done. In a section part, patient-specific data from an aortic dissection patient was used to develop of a FSI model, where the DFD method was applied and tested. More precisely, the imaging data, the model generation and the numerical model was briefly detailed. As we are still solving several numerical problems discussed earlier, the numerical problems have been presented and discussed along with some preliminary results.

Once I got used to the open-source software SimVascular [54], the implementation process went pretty smooth. Because the source code is very convoluted, the specific locations within the code must be determined in order to successfully implement the material model. Then, in a subsequent step, the input file has been generated and its format must be understood and followed. After this, the verification activities were successfully performed. However, first estimates showed that the computational time with the chosen DFD method in comparison with, for example, a neo-Hookean material model or a so-called Holzapfel-Gasser-Ogden model [17], both are implemented in SimVascular [54], increases significantly. Subsequently, an attempt was also made to optimize the source code and reduce the number of discrete elements in order to reduce the computation time with a view to later use in patient-specific geometries, which have significantly more degrees of freedom and therefore require a large amount of computation time.

With the support of Prof. Dominik Fleischmann, we were able to apply the implemented constitutive model to a patient-specific geometry of an aortic dissection, as previously detailed. After some internal iterations, models were generated from the computed tomography angiography scans, the models were meshed and boundary conditions were determined and set. Also, the simulations ran smoothly after applying a standard neo-Hookean material model. However, first trial simulations showed some numerical convergence issues related to the DFD method. Though, it was not clear if these problems were due to the material model itself, the mesh quality or others. After several discussions, we isolated the problem with several suggestion in order to resolve the problem in the nearer future.

In the future, this generated FSI model will be further investigated. As stated in the initial report, we will not be able to complete this project within the time framework of three month, since the task is just to comprehensive. However, we initiated this outstanding project and progressed very well over the last month. Now, after completing the research stay, we still work closely together in order to address and resolve the outline problems. Moreover, in the future, it is also planned to examine further follow-up computed tomography angiography images of this particular patient.

Acknowledgement

The work was supported by the Lead Project on ‘Mechanics, Modeling and Simulation of Aortic Dissection’, granted by Graz University of Technology, Graz, Austria. This work would not have been possible without the

support of Gerhard A. Holzapfel from Graz University of Technology, who acts as my supervisor. Moreover, an acknowledgment goes also to the research group of Alison L. Marsden and Dominik Fleischmann for the support provided during the research stay at Stanford University. Furthermore, an acknowledgement goes to the Austrian Marshall Plan Foundation for the Marshall Plan Scholarship n. 942121022222019.

References

[1] M. Alimohammadi, J. Sherwood, M. Karimpour, O. Agu, S. Balabani, and V. Díaz-Zuccarini. Aortic dissection simulation models for clinical support: fluid-structure interaction vs. rigid wall models. *Biomed Eng Online*, 14:34, 2015.

[2] K. Bäumler, V. Vedula, A. M. Sailer, J. Seo, P. Chiu, G. Mistelbauer, F. P. Chan, M. P. Fischbein, A. L. Marsden, and D. Fleischmann. Fluid–structure interaction simulations of patient-specific aortic dissection. *Biomech Model Mechanobiol*, 19:1607–1628, 2020.

[3] Y. Bazilevs, V. M. Calo, J. A. Cottrell, T. J. R. Hughes, A. Reali, and G. Scovazzi. Variational multiscale residual-based turbulence modeling for large eddy simulation of incompressible flows. *Comput Methods Appl Mech Eng*, 197:173–201, 2007.

[4] Y. Bazilevs, V. M. Calo, T. J. R. Hughes, and Y. Zhang. Isogeometric fluid-structure interaction: theory, algorithms, and computations. *Comput Mech*, 43:3–37, 2008.

[5] S. Bode-Jänisch, A. Schmidt, D. Günther, M. Stuhrmann, and A. Fieguth. Aortic dissecting aneurysms–histopathological findings. *Forensic Sci Int*, 214(1–3):13–7, 2012.

[6] B. L. Y. Cheuk and S. W. K. Cheng. Differential expression of elastin assembly genes in patients with Stanford type A aortic dissection using microarray analysis. *J Vasc Surg*, 53(4):1071–1078.e2, 2011.

[7] F. S. Cikach, C. D. Koch, T. J. Mead, J. Galatioto, B. B. Willard, K. B. Emerton, M. J. Eagleton, E. H. Blackstone, F. Ramirez, E. E. Roselli, and S. S. Apte. Massive aggrecan and versican accumulation in thoracic aortic aneurysm and dissection. *JCI Insight*, 3(5), 2018.

[8] L. de Figueiredo Borges, J. P. F. Blini, R. R. Dias, and P. S. Gutierrez. Why do aortas cleave or dilate? clues from an electronic scanning microscopy study in human ascending aortas. *J Vasc Res*, 51(1):50–7, 2014.

[9] L. de Figueiredo Borges, Z. Touat, A. Leclercq, A. Al Haj Zen, G. Jondeau', B. Franc, M. Philippe, O. Meilhac, P. S. Gutierrez, and J.-B. Michel. Tissue diffusion and retention of metalloproteinases in ascending aortic aneurysms and dissections. *Hum Pathol*, 40(3):306–13, 2009.

[10] R. Erbel, F. Alfonso, C. Boileau, O. Dirsch, B. Eber, A. Haverich, H. Rakowski, J. Struyven, K. Radegran, U. Sechtem, J. Taylor, C. Zollikofer, W. W. Klein, B. Mulder, and L. A. Providencia. Diagnosis and management of aortic dissection. *Eur Heart J*, 22(18):1642–81, 2001.

[11] J. Erdheim. Medionecrosis aortae idiopathica. *Virch Arch Pathol Anat*, 273:454–479, 1929.

[12] M. Esmaily-Moghadam, Y. Bazilevs, and A. L. Marsden. A new preconditioning technique for implicitly coupled multidomain simulations with applications to hemodynamics. *Comput Mech*, 52:1151–1152, 2013.

[13] M. Esmaily-Moghadam, Y. Bazilevs, and A. L. Marsden. A bi-partitioned iterative algorithm for solving linear systems arising from incompressible flow problems. *Comput Methods Appl Mech Eng*, 286:40–62, 2015.

[14] D. Fleischmann, R. Afifi, A. Casanegra, J. Elefteriades, T. Gleason, K. Hanneman, E. Roselli, M. Willemink, and M. Fischbein. Imaging and surveillance of chronic aortic dissection: a scientific statement from the American Heart Association. *Circ Cardiovasc Imaging*, 15(3):e000075, 2022.

[15] P. G. Hagan, C. A. Nienaber, E. M. Isselbacher, D. Bruckman, D. J. Karavite, P. L. Russman, A. Evangelista, R. Fattori, T. Suzuki, J. K. Oh, A. G. Moore, J. F. Malouf, L. A. Pape, C. Gaca, U. Sechtem, S. Lenferink, H. Deutsch, H. Diedrichs, J. Marcos y Robles, A. Llovet, D. Gilon, D. S. K., W. F. Armstrong, G. M. Deeb, and K. Eagle. The international registry of acute aortic dissection (IRAD): new insights into an old disease. *JAMA*, 283(7):897–903, 2000.

[16] L. F. Hiratzka, G. L. Bakris, J. Beckman, R. M. Bersin, V. F. Carr, D. E. J. Casey, K. A. Eagle, L. K. Hermann, E. M. Isselbacher, E. A. Kazerooni, N. T. Kouchoukos, B. W. Lytle, D. M. Milewicz, D. L. Reich, S. Sen, J. A. Shinn, L. G. Svensson, and D. M. Williams. ACCF/AHA/AATS/ACR/ASA/SCA/SCAI/SIR/STS/SVM Guidelines for the diagnosis and management of patients with thoracic aortic disease. a report of the american college of cardiology foundation/american heart association task force on practice guidelines, american association for thoracic surgery, american college of radiology,american stroke association, society of cardiovascular anesthesiologists, society for cardiovascular angiography and interventions, society of interventional radiology, society of thoracic surgeons,and society for vascular medicine. *J Am Coll Cardiol*, 55(14):e27–e129, 2010.

[17] G. A. Holzapfel, T. C. Gasser, and R. W. Ogden. A new constitutive framework for arterial wall mechanics and a comparative study of material models. *Journal of elasticity and the physical science of solids*, 61(1):1–48, 2000.

[18] G. A. Holzapfel, J. A. Niestrawska, R. W. Ogden, A. R. Reinisch, and A. J. Schriefl. Modelling non-symmetric collagen fibre dispersion in arterial walls. *J R Soc Interface*, 12(106):1–14, 2015.

[19] G. A. Holzapfel and R. W. Ogden. On the tension– compression switch in soft fibrous solids. *Eur J Mech A/Solids*, 49:561–569, 2015.

[20] G. A. Holzapfel, C. A. J. Schulze-Bauer, and M. Stadler. Mechanics of angioplasty: wall, balloon and stent. In J. Casey and G. Bao, editors, *Mechanics in Biology*, New York, 2000. The American Society of Mechanical Engineers (ASME). AMD-Vol. 242/BED-Vol. 46, pp. 141–156.

[21] G. A. Holzapfel, G. Sommer, C. T. Gasser, and P. Regitnig. Determination of layer-specific mechanical properties of human coronary arteries with nonatherosclerotic intimal thickening and related constitutive modeling. *Am J Physiol Heart Circ Physiol*, 289(5):H2048–58, 2005.

[22] M.-C. Hsu and Y. Bazilevs. Blood vessel tissue prestress modeling for vascular fluid–structure interaction simulation. *Finite Elem Anal Des*, 47(6):593–599, 2011.

[23] E. M. Isselbacher, O. Preventza, J. H. Black, J. G. Augoustides, A. W. Beck, M. A. Bolen, A. C. Braverman, B. E. Bray, M. M. Brown-Zimmerman, E. P. Chen, T. J. Collins, A. DeAnda, C. L. Fanola, L. N. Girardi, C. W. Hicks, D. S. Hui, W. Schuyler Jones, V. Kalahasti, K. M. Kim, D. M. Milewicz, G. S. Oderich, L. Ogbechie, S. B. Promes, E. G. Ross, M. L. Schermerhorn, S. S. Times, E. E. Tseng, G. J. Wang, and Y. J. Woo. 2022 ACC/AHA Guideline for the diagnosis and management of aortic disease: a report of the American Heart Association/American College of Cardiology Joint Committee on Clinical Practice Guidelines. *J Am Coll Cardiol*, 80:e223–e393, 2022.

[24] H. J. Kim, I. E. Vignon-Clementel, C. A. Figueroa, K. E. Jansen, and C. A. Taylor. Developing computational methods for three-dimensional finite element simulations of coronary blood flow. *Finite Elem Anal Des*, 46:514–525, 2010.

[25] W. K. Laskey, H. G. Parker, V. A. Ferrari, W. G. Kussmaul, and A. Noordergraaf. Estimation of total systemic arterial compliance in humans. *J Appl Physiol (1985)*, 69:112–119, 1990.

[26] K. Li, R. W. Ogden, and G. A. Holzapfel. Computational method for excluding fibers under compression in modeling soft fibrous solids. *Eur J Mech A-Solid*, 57:178–193, 2016.

[27] K. Li, R. W. Ogden, and G. A. Holzapfel. A discrete fibre dispersion method for excluding fibres under compression in the modelling of fibrous tissues. *J R Soc Interface*, 15(138), 2018.

[28] K. Li, R. W. Ogden, and G. A. Holzapfel. An exponential constitutive model excluding fibres under compression: application to extension–inflation of a residually stressed carotid artery. *Math Mech Solids*, 23(8):1206–1224, 2018.

[29] P. Moireau, C. Bertoglio, N. Xiao, C. A. Figueroa, C. A. Taylor, D. Chapelle, and J. F. Gerbeau. Sequential identification of boundary support parameters in a fluid-structure vascular model using patient image data. *Biomech Model Mechanobiol*, 12:475–496, 2013.

[30] P. Moireau, N. Xiao, M. Astorino, C. A. Figueroa, D. Chapelle, C. A. Taylor, and J. F. Gerbeau. External tissue support and fluid-structure simulation in blood flows. *Biomech Model Mechanobiol*, 11:1–18, 2012.

[31] Y. Nakashima. Pathogenesis of aortic dissection: elastic fiber abnormalities and aortic medial weakness. *Ann Vasc Dis*, 3(1):28–36, 2010.

[32] W. W. Nichols and M. F. O'Rourke. Taylor & Francis, London, 2005.

[33] M. K. O'Connell, S. Murthy, S. Phan, C. Xu, J. Buchanan, R. Spilker, R. L. Dalman, C. K. Zarins, W. Denk, and C. A. Taylor. The three-dimensional micro- and nanostructure of the aortic medial lamellar unit measured using 3D confocal & electron microscopy imaging. *Matrix Biol*, 27(3):171–81, 2008.

[34] S. Pasta, J. A. Phillippi, T. G. Gleason, and D. A. Vorp. Effect of aneurysm on the mechanical dissection properties of the human ascending thoracic aorta. *J Thorac Cardiovasc Surg*, 143(2):460–7, 2012.

[35] P. D. Patel and R. R. Arora. Pathophysiology, diagnosis, and management of aortic dissection. *Ther Adv Cardiovasc Dis*, 2(6):439–68, 2008.

[36] S. Ranftl, M. Rolf-Pissarczyk, G. Wolkerstorfer, A. Pepe, J. Egger, W. von der Linden, and G. A. Holzapfel. Stochastic modeling of inhomogeneities in the aortic wall and uncertainty quantification using a bayesian encoder-decoder surrogate. *Comput Methods Appl Mech Eng*, 401:115594, 2022.

[37] P. Reymond, P. Crosetto, S. Deparis, A. Quarteroni, and S. N. Physiological simulation of blood flow in the aorta: comparison of hemodynamic indices as predicted by 3-D FSI, 3-D rigid wall and 1-D models. *Med Eng Phys*, 35:784–791, 2013.

[38] M. Rolf-Pissarczyk, K. Li, D. Fleischmann, and G. A. Holzapfel. A discrete approach for modeling degraded elastic fibers in aortic dissection. *Comput Methods Appl Mech Eng*, 373:113511, 2021.

[39] M. Rolf-Pissarczyk, M. P. Wollner, D. R. Q. Pacheco, and G. A. Holzapfel. Efficient computational modelling of smooth muscle orientation and function in the aorta. *Proc R Soc A*, 477:20210592, 2021.

[40] E. B. Rosero, R. M. Peshock, A. Khera, P. Clagett, H. Lo, and C. H. Timaran. Sex, race, and age distributions of mean aortic wall thick- ness in a multiethnic population-based sample. *J Vasc Surg*, 53:950—–957, 2011.

[41] A. Schriefl, G. Zeindlinger, D. Pierce, P. Regitnig, and G. A. Holzapfel. Determination of the layer-specific distributed collagen fibre orientations in human thoracic and abdominal aortas and common iliac arteries. *J R Soc Interface*, 9(71):1275–1286, 2012.

[42] R. Schussnig, K. Bäumler, and T.-P. Fries. Multi-layered tissue models in patient-specific simulations of aortic dissection. In *Proc Appl Math Mech*, volume 21, page e202100090, 2021.

[43] R. Schussnig and T.-P. Fries. Coupled multiphysics modeling of aortic dissection. In *14th WCCM ECCOMAS Congress 2020, Virtual Congress*, 2020.

[44] R. Schussnig, D. Pacheco, and T.-P. Fries. Efficient split-step schemes for fluid–structure interaction involving incompressible generalised ßnewtonian flows. *Comput. Struct*, 260:106718, 2022.

[45] R. Schussnig, D. R. Q. Pacheco, M. Kaltenbacher, and T. P. Fries. Semi-implicit fluid–structure interaction in biomedical applications. *Comput Methods Appl Mech Eng*, 400:115489, 2022.

[46] R. Schussnig, M. Rolf-Pissarczyk, G. A. Holzapfel, and T. P. Fries. Fluid-structure interaction simulations of aortic dissection. In *Proc Appl Math Mech*, volume 20, 2020.

[47] J. Seo, D. E. Schiavazzi, and A. L. Marsden. Performance of preconditioned iterative linear solvers for cardiovascular simulations in rigid and deformable vessels. *Comput Mech*, 64:717–739, 2019.

[48] S. Sherifova and G. A. Holzapfel. Biomechanics of aortic wall failure with a focus on dissection and aneurysm: a review. *Acta Biomater*, 99:1–17, 2019.

[49] H. Si. Adaptive tetrahedral mesh generation by constrained delaunay refinement. *Int J Numer Meth Eng*, 75:856–880, 2008.

[50] J. C. Simo and R. L. Taylor. Quasi-incompressible finite elasticity in principal stretches. Continuum basis and numerical algorithms. *Comput Meth Appl Mech Eng*, 85(3):273–310, 1991.

[51] K. Takizawa, T. E. Tezduyar, and T. Sasaki. Estimation of element-based zero-stress state in arterial fsi computations with isogeometric wall discretization. *Lect Notes Appl Comput Mech*, 84:101–122, 2018.

[52] T. E. Tezduyar, S. Mittal, S. E. Ray, and R. Shih. Incompressible flow computations with stabilized bilinear and linear equal-order-interpolation velocity-pressure elements. *Comput Methods Appl Mech Eng*, 95:221–242, 1992.

[53] T. E. Tezduyar, S. Sathe, M. Schwaab, and B. S. Conklin. Arterial fluid mechanics modeling with the stabilized space-time fluid—structure interaction technique. *Int J Numer Methods Fluids*, 57:601–629, 2008.

[54] A. Updegrove, N. M. Wilson, J. Merkow, H. Lan, A. L. Marsden, and S. C. Shadden. SimVascular: an open source pipeline for cardiovascular simulation. *Ann Biomed Eng*, 45:525–541, 2016.

[55] W. N. Wan Ab Naim, P. B. Ganesan, Z. Sun, K. H. Chee, S. A. Hashim, and L. Einly. A perspective review on numerical simulations of hemodynamics in aortic dissection. *ScientificWorldJournal*, 2014:652520, 2014.

[56] L. Wang, J. Zhang, W. Fu, D. Guo, J. Jiang, and Y. Wang. Association of smooth muscle cell phenotypes with extracellular matrix disorders in thoracic aortic dissection. *J Vasc Surg*, 56(6):1698–709, 1709.e1, 2012.

[57] X. Wang, S. A. LeMaire, L. Chen, Y. H. Shen, Y. Gan, H. Bartsch, S. A. Carter, B. Utama, H. Ou, J. S. Coselli, and X. L. Wang. Increased collagen deposition and elevated expression of connective tissue growth factor in human thoracic aortic dissection. *Circulation*, 114(1 Suppl):I200–5, 2006.

[58] D. Wu, Y. H. Shen, L. Russell, J. S. Coselli, and S. A. LeMaire. Molecular mechanisms of thoracic aortic dissection. *J Surg Res*, 184(2):907–24, 2013.

[59] Y. Zhu, S. Mirsadraee, U. Rosendahl, J. Pepper, and X. Y. Xu. Fluid-structure interaction simulations of repaired type A aortic dissection: a comprehensive comparison with rigid wall models. *Front Physiol*, 13:913457, 2022.

[60] J. Zimmermann, K. Bäumler, M. Loecher, T. E. Cork, A. L. Marsden, D. Fleischmann, and D. B. Ennis. Hemodynamic effects of tear size in aortic dissections: comparing in vitro flow magnetic resonance imaging with fluid-structure interaction simulations. *Sci Rep*, 2023.